$\mathcal{R}$esearch in
$\mathcal{A}$stronomy and
$\mathcal{A}$strophysics

A solar radio dynamic spectrograph with flexible temporal-spectral resolution

Qing-Fu Du[1,2], Lei Chen[1], Yue-Chang Zhao[1], Xin Li[1], Yan Zhou[1], Jun-Rui Zhang[1], Fa-Bao Yan[1,2], Shi-Wei Feng[2], Chuan-Yang Li[2] and Yao Chen[2]

[1] School of Mechanical, Electrical & Information Engineering, Shandong University, Weihai 264209, China; *dqf@sdu.edu.cn*

[2] Institute of Space Sciences, Shandong University, Weihai 264209, China; *hjc-8555@sdu.edu.cn*

Abstract Observation and research on solar radio emission have unique scientific values in solar and space physics and related space weather forecasting applications, since the observed spectral structures may carry important information about energetic electrons and underlying physical mechanisms. In this study, we present the design of a novel dynamic spectrograph that has been installed at the Chashan Solar Radio Observatory operated by the Laboratory for Radio Technologies, Institute of Space Sciences at Shandong University. The spectrograph is characterized by real-time storage of digitized radio intensity data in the time domain and its capability to perform off-line spectral analysis of the radio spectra. The analog signals received via antennas and amplified with a low-noise amplifier are converted into digital data at a speed reaching up to 32 k data points per millisecond. The digital data are then saved into a high-speed electronic disk for further off-line spectral analysis. Using different word lengths (1–32 k) and time cadences (5 ms–10 s) for off-line fast Fourier transform analysis, we can obtain the dynamic spectrum of a radio burst with different (user-defined) temporal (5 ms–10 s) and spectral (3 kHz∼320 kHz) resolutions. This enables great flexibility and convenience in data analysis of solar radio bursts, especially when some specific fine spectral structures are under study.

Key words: Sun: radio radiation — radiation: dynamics — instrumentation: spectrographs — methods: data analysis — techniques: image processing

1 INTRODUCTION

There exist different types of solar radio bursts (defined as a transient enhancement of intensities at radio frequencies), spanning several decades from the microwave regime to metric-kilometric wavelengths. These radio bursts are released by energetic electrons accelerated during solar eruptions (e.g. flares and coronal mass ejections), through emitting mechanisms like plasma emission, thermal bremsstrahlung (free-free) emission, synchrotron emission, as well as cyclotron maser emission, among other possibilities (Wild & McCready 1950; Melrose 1980; McLean & Labrum 1985). Of particular interest here is solar metric radio bursts that are associated with energetic electrons in the corona (see Feng et al. 2013, 2015, 2016; Kong et al. 2012, 2016; Chen

et al. 2014; Vasanth et al. 2016; Du et al. 2014, 2015; Koval et al. 2016; Gao et al. 2016, for the latest studies). How these electrons are accelerated and how the emission is generated remain elusive. Observations and scientific studies of solar radio bursts, of interest in their own aspects, can provide valuable diagnostic information on energetic electrons, as well as coronal plasmas and the embedded magnetic field strengths and configurations, which remain major challenges with present techniques. Thus, it is a crucial task of the solar and space physics-space weather communities to develop a state-of-the-art technological system to detect and analyze solar radio bursts.

These bursts are traditionally measured by solar radio spectrographs, which can yield dynamic spectra within a broad band of frequencies. Tens of such systems

have been established around the world. Table 1 shows parameters of some solar radio observing systems. Most early solar radio spectrographs provide data with fixed spectral and temporal resolution. One of the latest radio observational systems was built by Yunnan Observatories in 2012, with a maximum temporal resolution reaching up to 2 ms, and a frequency resolution of ∼200 kHz (Gao et al. 2014). This system employs electronic switches to transfer between right-handed and left-handed polarized signals, to reduce system cost. Its working frequency is from 70 to 700 MHz with a 11 m parabolic antenna fed by a crossed log-periodic dipole antenna (LPDA).

Many systems listed in Table 1 use the extended Compact Astronomical Low-cost Low-frequency Instrument for Spectroscopy and Transportable Observatory (e-CALLISTO) spectrograph (Benz et al. 2005, 2009), which is designed mainly for economic considerations. In addition, the relevant antenna system usually lacks high sensitivity. Therefore, observational data from e-CALLISTO systems, although very valuable with their worldwide distribution that provides 24-hour tracking of the Sun, often yield noisy spectral data with temporal and spectral resolutions fixed and relatively low.

Other radio spectrograph systems, e.g., the Green Bank Solar Radio Burst Spectrograph (GBSRBS: *http://www.astro.umd.edu/∼white/gb/*) and the Hiraiso Radio Spectrograph (Kondo et al. 1994), were mostly built 10 to 20 years ago, when electronic devices and computer technology suffered from major limitations. For instance, the analog-to-digital converter (ADC) sampling rate was usually at the rate of 10s to 100 MHz. According to the Nyquist sampling theorem, the sampling rate should be at least twice the signal bandwidth. Therefore, to observe a wide-band (e.g., 150∼500 MHz) solar radio burst, one has to split the total bandwidth into several segments and assemble them later (e.g. Fu et al. 2004). This introduces considerable complexity (and thus noise and cost) to the system and puts a strong limitation on data quality.

Most, if not all, earlier solar radio spectrographs are providing data with fixed spectral and temporal resolutions. In principle, the temporal and spectral resolutions of these data can still be changed by averaging the data within a certain period (or frequency interval). This always reduces the resolution of the data. Here we propose a novel design for a solar radio spectrograph, characterized by high-speed real-time storage of digitized data in the time domain and offline analysis with flexible temporal and spectral resolutions. The system is based on high-speed wide-band ADCs and hardware computation using a field-programmable gate array (FPGA). The sampling speed of the ADC is 1 GHz (12 bits). This allows us to sample the radio signals below 500 MHz with only one ADC, and greatly simplifies the design of the system. It is suggested that this novel system will be helpful to further explore the scientific potential of radio spectral data, especially for studies on fine spectral structures.

In the following, we first present two related concepts used in the study, then we introduce the Chashan Solar Radio Observatory (CSO), the data acquisition system (DAS) of the spectrograph and the calibration methods. The design of the spectrograph is demonstrated by showing spectral analyses of two solar radio burst events. The last section summarizes this paper.

2 THE SPECTROGRAPH NOISE FLOOR AND FFT ANALYSIS WITH DIFFERENT WORD LENGTHS

In this section, we briefly introduce the concepts of the noise floor of a spectrograph and fast Fourier transform (FFT) analysis with different word lengths, which are closely related to our study.

A radio spectrograph can only detect signals with energies above its system noise floor (p_n), given by

$$
\begin{aligned}
p_n &= \lg(kTB) + N_F \\
&= 10\lg(kT) + 10\lg(B) + N_F \\
&= -174 + 10\lg(B) + N_F,
\end{aligned}
\tag{1}
$$

where N_F is the noise figure of the system, the temperature T is taken to be 290 K, and B is the observing bandwidth, k is the Boltzmann constant (1.38×10^{-23} J K^{-1}) and p_n is in units of dBm Hz^{-1}. We can see that at a fixed temperature, p_n is smaller when N_F and B are smaller. It is in general important to reduce the value of p_n in order to observe weaker signals.

FFT is an efficient algorithm that implements the transform from time domain to frequency domain. The frequency (or spectral) resolution can be determined with the following expression

$$
\Delta f = k \times \frac{F_s}{N},
\tag{2}
$$

where F_s is the total bandwidth of the signal, N is the word length of the FFT operation (or the sampling rate, the number of sampled points), and k is the coefficient given by a window function. We see that Δf is inversely proportional to N. To detect a signal with specific fine spectral structures, sufficiently high spectral (and temporal) resolution is required. Yet, it should be noted that

Table 1 Parameters of Solar Radio Observing Systems around the World

Station name/Country /Construction time	Latitude and longitude/Observation time	Antennas	Observation frequency band (MHz)	Time resolution (s)	Frequency resolution (channel number) (Hz)
AMATERAS /Japan/2010	E141N38 20–06 UT	$2 \times 16.5 \times 31$ m of a rectangular paraboloid: 1023 m^2	150–500	0.01	61 kHz (16 384 channels)
BIRS[1]/Australia /1997	E147S43 20–06 UT	23 element log-periodic structure	5–65	3	268 kHz
Artemis[2] IV/Greece /1996	E22N38.5 (06– 16 UT)	7 m paraboloid + LPDA (100–650 MHz); Anti-V-shaped dipole antenna (20–100 MHz)	20–100, 100–650	0.1, 0.01 (270–450)	1. 630 channels (20–650) 2. 128 channels (270–450)
OOTY[3]- Callisto/ India	E76N11 02–12UT	Linear polarization single group (LPDA)	45–870	0.25	200 channels
Bleie[4]/ Switzerland	E8N47 (06–16)	7 m paraboloid, LPDA	170–870	0.25	200 channels
GBSRBS/ US /2004	W79N38	10–80: LPDA 80–850: 13.7 m 800–3000: 3 m	10–3000	1	
San Vito/ Italy	E18N41 (06–16)	Non-tracking Semi-Bicone, LPDA	25–75, 75–180	3	HP 8591E Spectrum analyzer
Yunnan Observatory[5]	102E,24N	11 m parabolic antenna	70–700	0.002	200 kHz
Chashan Solar Radio Observatory	122E,36N	6 m parabolic antenna	150–500	0.005– 0.01	3 k–320 k (flexible)

Notes: [1]Bill Erickson and Hilary Cane's BIRS system on Bruny Island suffered a serious hardware failure in January 2015 and may not be reparable, so there have been no new BIRS data since then. [2]*http://artemis-iv.phys.uoa.gr/Artemis4_list.html*; [3]*http://www.e-callisto.org/*; [4]*http://soleil.i4ds.ch/solarradio/*; [5]*http://secchirh.obspm.fr/instruments.php#ynao*

both the temporal and spectral resolutions cannot be increased unlimitedly due to the limited energy of the signal. The window function, usually bell-shaped, reduces signal distortions and spectral energy dispersions, which may be introduced between successive frames due to the FFT operations with limited data. In addition, with a larger N and thus a smaller Δf, the power of the background emission (i.e., the noise) should decrease accordingly, which effectively reduces the noise floor, as illustrated in the spectral analysis.

3 THE CSO, DAS AND CALIBRATION METHODS

3.1 A Brief Introduction to the CSO

Construction of the CSO started in 2015. First light (observing a solar radio burst) was received in July 2016. The observatory is located on Chashan Mountain in Rongcheng City, on the southernmost part of the Jiaodong Peninsula, and is operated by the Laboratory for Radio Technologies, Institute of Space Sciences, Shandong University. The spectral band of interest here is from 150 to 500 MHz, observed with a 6 m parabola fed by a crossed LPDA, which can track the Sun automatically from 6 AM to 5 PM local time in summer

and from 8 AM to 5 PM in winter. The northern part of the site is the mountain with an altitude up to 500 m; the southern part is the Yellow Sea; the eastern and western parts are partially surrounded by mountains. Therefore, this site has the advantage of low radio frequency interference (RFI). This is an extremely important factor for successful observation of solar radio bursts at the metric wavelength, as verified by on-going observations.

3.2 Data Acquisition System

The core part of the data acquisition system (DAS) is a high-speed acquisition card, with a 2-channel synchronous 12 bit 1 Gigabit Samples Per Second (GSPS) ADC and 4 GB of high-speed DDR3 cache memory, and a Xilinx XC6VSX315T FPGA chip. The card supports 8-channel and up to 32 k (N) synchronous real-time FFT processing. The system also supports a PCIe 2.0 x8 bus with data transmission speed as large as 2.5 GB s^{-1}. The programs related to this study are executed on this card. The diagram in Figure 1 shows the main functions of the spectrograph.

The signals, received by the antenna and processed by the low-noise amplifier (LNA), are converted into digital data via the ADC. We use four First-In First-Out (FIFO) registers to decelerate the data flow to $\frac{1}{4}$ of the
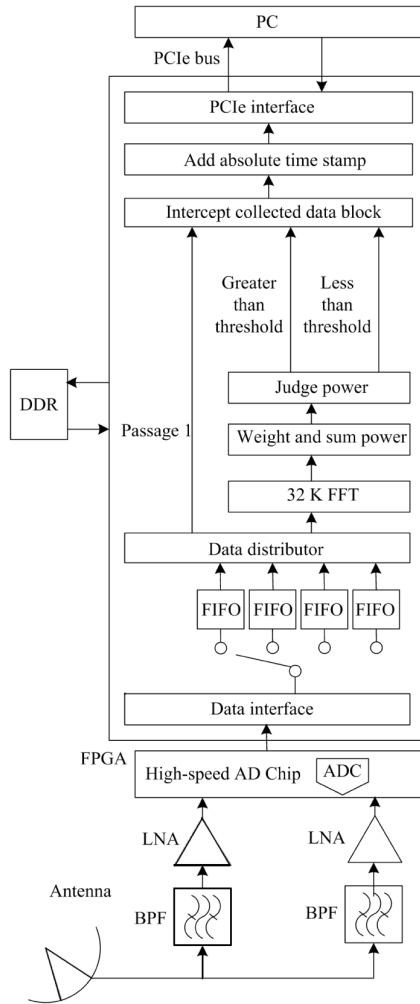
Fig. 1 The system block diagram.

original speed. The FFT functions for the data received through the four registers are performed independently. The obtained results are then combined to form a full spectrum. To reduce the influence of RFI, we find out the known channels of RFI and set the signal to zero there. Then we sum up the total energy within the observing band to give the weighted total power of the spectrum (It). When the obtained It is larger (smaller) than a prescribed threshold, the system works in burst (normal) mode. The threshold is determined by observational tests.

In normal mode, the cadence of data collection is relatively low. For instance, we can set the system to collect 32 k data points per second. However in burst mode, the system works to its full potential, and 32 k data points will be collected per millisecond. In each mode, real-time

dynamic spectra will be saved (together with the time stamps) to produce a synoptic spectrum. In the meantime, the output digital data (in the time domain) of the ADC (together with the time stamps) will be saved onto a high-speed electronic hard disk for further off-line analysis. Note that in the above setup of the burst mode, one can obtain a huge amount of data, $\sim$96 GB, in 10 min.

To store the huge amount of digitized time-domain data during burst mode, we set up a 4 GB DDR3 cache memory with two data blocks (A and B). The volume of A or B is configured according to the amount of the data that need to be saved. The FPGA chip is linked directly to the high-speed PCIE bus of the computer. Data from the ADC and the FFT results of the FPGA are first buffered in the blocks, and then uploaded to the computer via the ping-pong method. In other words, the data are first saved in block A, and uploaded when A is full; during the uploading process, data will be saved in block B, and uploaded when it is full; then data will be saved in A again, and so on. In addition, we need to make sure that the uploading speed is always larger than the data acquisition speed to avoid loss of data. The data package on the computer will be named according to the data and the exact time of the package. Usually, the system is set to collect and save the data automatically during daytime, and after sunset, the data will be examined manually to remove the data of no interest (e.g. without any signature of radio bursts) to save space.

The control software of the spectrograph is developed with the Microsoft Foundation Class Library and installed on the host computer. Through the software, the user can select data channels, set the temporal resolution, adjust the power threshold to determine the running mode of the system (i.e., normal or burst), perform file operations, etc.

3.3 Data Calibration

We have currently designed two calibration methods. The first one has been implemented and the second one is still under construction. The former is presented as follows.

The Learmonth Radio Observatory releases calibrated solar radio flux intensity at several discrete frequencies (from 245 MHz to 15 400 MHz). One can use these open-access data for calibration. The 245 MHz is within the observational range of the CSO spectrograph, therefore the data at this frequency can be calibrated. To do this, we apply the following algorithm to the value R that is the spectral intensity at the selected frequency in arbitrary unit,

$$F_A = A \times \lg \left[(R - B) \times C \right]. \tag{3}$$

By adjusting parameters A, B and C, we make sure that the deduced F_A within a certain period is basically the same as that given by Learmonth (F). A comparison of the two curves can be seen in Figure 2. We have $A = 1.0040$, $C = 0.2890$ and $B = 572.5720$. To test this calibration method, we repeat the above calculation (with the same set of coefficients) for the radio flux data obtained the next day (2016 July 19). A consistent result is found (see Fig. 2b). This indicates the success of this calibration method. In practice, the coefficients (A, B, C) should be corrected every day to ensure a proper calibration.

Another calibration method is usually referred to as the Y-factor method (see, e.g., Tan et al. 2015). This method utilizes a standard noise source with a known power of output signal in white noise. With this method, the front-end electronics system and the receiver (all electronic devices after the antenna) can be calibrated (see Fig. 3). The antenna properties should be tested and calibrated independently. A noise generator with an Excess Noise Ratio (ENR) of 30 dB and a 50 Ohm resistor are used for the calibration.

The temperature (T_{ENR}) of the 30 dB ENR noise source can be calculated through

$$P_{ENR} = 10 \lg \left(\frac{T_{ENR}}{T_0} - 1 \right), \qquad (4)$$

where T_0 is the room temperature and $P_{ENR} = 30$ dB. The receiver reads P_{T_0} when connected to the 50 Ohm resistor, and reads P_{ENR} when connected to the noise source, and the system temperature of the receiver is T_{SYS}. One has

$$P_{ENR} = \frac{T_{ENR} - Y \times T_0}{Y - 1}, \qquad (5)$$

$$G = \frac{T_{ENR}}{kB(T_{SYS} - T_0)}, \qquad (6)$$

where G is the gain of the receiver and $Y = \frac{P_{T_{ENR}}}{P_{T_0}}$. Note that this calibration method should be used together with the test and calibration of the antenna-feed system (not finished yet).

4 OFFLINE ANALYSIS OF THE DATA

As introduced earlier, the spectral resolution is directly determined by the word length N of the FFT analysis. When N increases by a factor of 10, so does the spectral resolution. For example, with a sampling frequency being 1 GSPS, $N = 32$ k corresponds to a frequency resolution of $\sim$30 kHz, and $N = 320$ k corresponds to a frequency resolution of $\sim$3 kHz. In addition, with a larger N, smaller values of the system noise floor can be obtained. In the following we demonstrate this effect of N on the FFT analysis with two solar radio burst events recorded by the CSO spectrograph on 2016 July 18 and 2016 July 19 respectively. The data sampling is at a cadence of 10 ms with 32 k data points being collected at each sampling.

Figure 4 shows a comparison between dynamic spectra with $N = 1$ k and 32 k ($\Delta f = \sim$1 MHz and $\sim$30 kHz respectively) with the same temporal resolution ($\Delta t = 250$ ms). The full spectra from 150 to 500 MHz are shown in the upper panels with different contrast. Note the color of the background emission of the two panels has been adjusted to be close to each other, for convenience of comparison. The lower two panels of Figure 4 show the spectra observed from 225 to 235 MHz. In both panels (b) and (d), the background level is weaker by about 15 dBm due to a larger N (32 k versus 1 k). This figure clearly demonstrates the effect of N on the noise floor of the system.

To show the comparison in a more quantitative way, we plot the flux curves at 305 MHz in the upper panels of Figure 5. The data are shown for different temporal resolutions (50 ms and 250 ms) as well as different FFT word lengths (1 k and 32 k). We see that the data with 250 ms display a slightly lower noise floor by $\sim$2 dBm than that of $\Delta t = 50$ ms (with the same N), and the data with $N = 1$ k exhibit a much larger noise floor by $\sim$15 dBm than that of $N = 32$ k (with the same Δt).

In the lower panels of Figure 5, we show the signal to noise ratio (SNR) of the data. The SNR is calculated with the following equation,

$$\text{SNR} = 10 \lg \left(\frac{P_s}{P_n} \right) \text{(dB)}, \qquad (7)$$

where P_s is the power of the signal and the noise floor of the spectrograph P_n is represented by the root mean square (RMS) of the fluctuating power of the background signal. We see that although the noise floor of different parameters is very different, the SNRs are quite similar to each other. This is due to the fact that the powers of both the signals and the background noises change accordingly with the spectral and temporal resolutions.

To demonstrate the capability of the CSO spectrograph in identifying fine spectral structures, in Figure 6 we show two sets of dynamic spectra observed on 2016 July 18 (the same event reported above) and 2016 July 19, respectively. Each event is shown for $N = 1$ k and $N = 32$ k with the spectral resolution being 1 MHz and 30 kHz. The contrast levels of the spectra with different N have been adjusted to reveal a similar color of the background emission.
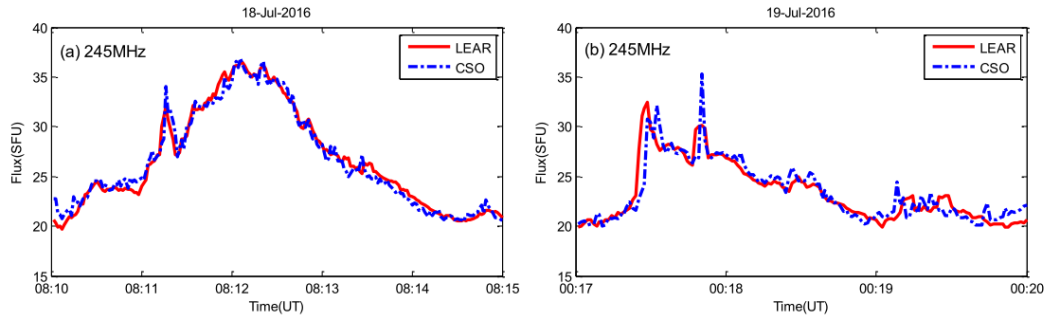
Fig. 2 Comparison of the calibrated data obtained by the CSO spectrograph and those released by the Learmonth Radio Observatory in Australia at 245 MHz.
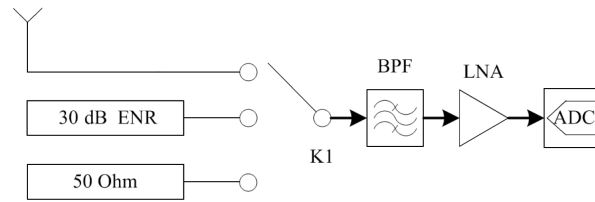

Fig. 3 The Y-factor method of spectrograph calibration, using a standard noise source with 30 dB ENR.
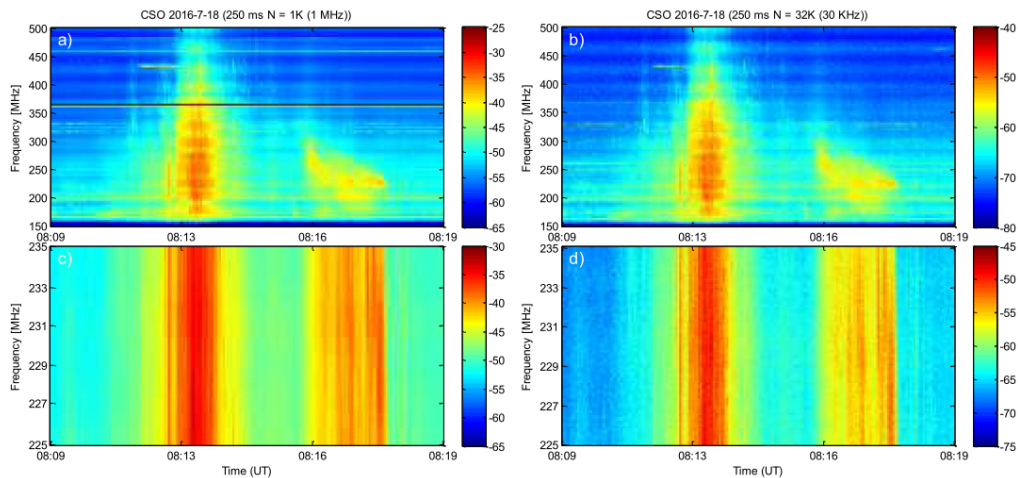

Fig. 4 The solar type III and type IV radio bursts on 2016 July 18 observed by the CSO, shown for comparison with spectra having different FFT word lengths (1 k and 32 k) with the same temporal resolution (250 ms). The spectral resolution is about 1 MHz for $N = 1$ k and about 30 kHz for $N = 32$ k, as written in the parentheses.

In panels (a) and (d) of Figure 6, we see that there are observable mosaic patterns due to the low frequency resolution, while in panels (b) and (e) such mosaic patterns are removed due to the increased spectral resolution. In addition, the filamentary fine structures and their drifting trend/rate can only be clearly discernible from panels (b) and (e). See the regions outlined by white rectangles. Panels (c) and (f) show the dynamic spectra with frequency resolution of 3 kHz ($N = 320$ k) that is the highest resolution available with the CSO spectrograph. Note

that in order to have enough energy at each data point, we use a low time resolution of 960 ms. Compared with Figure 4, the noise floor is much lower at the frequency resolution of 3 kHz, by 10 dBm than that at $N = 32$ k and $\Delta t = 250$ ms, and by 25 dBm than that at $N = 1$ k and $\Delta t = 250$ ms. Nevertheless, the energy at each data point is quite limited by this super-high spectral resolution. This affects the quality of the spectra, indicating that indeed the resolutions (spectral or temporal) cannot be increased unlimitedly.
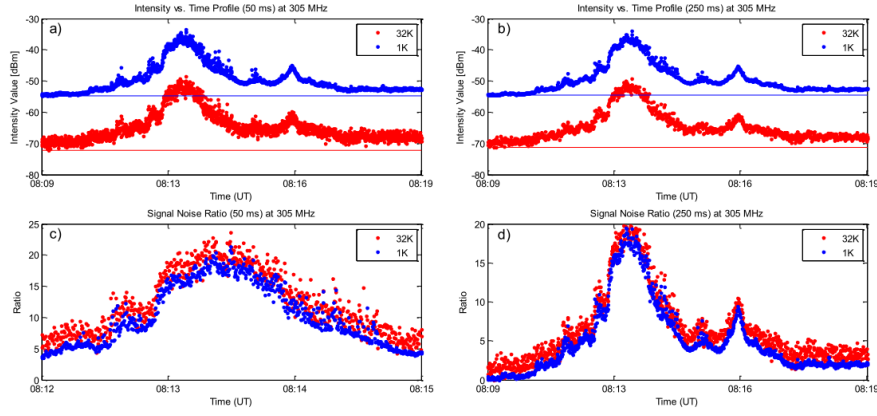
Fig. 5 Panels (a) and (b) show the flux intensity curves at 305 MHz, with different temporal resolutions (50 ms and 250 ms) and different FFT word lengths (1 k and 32 k), and (c) and (d) show the corresponding SNRs. The horizontal lines represent the corresponding noise floors given by the RMS of the background intensity.
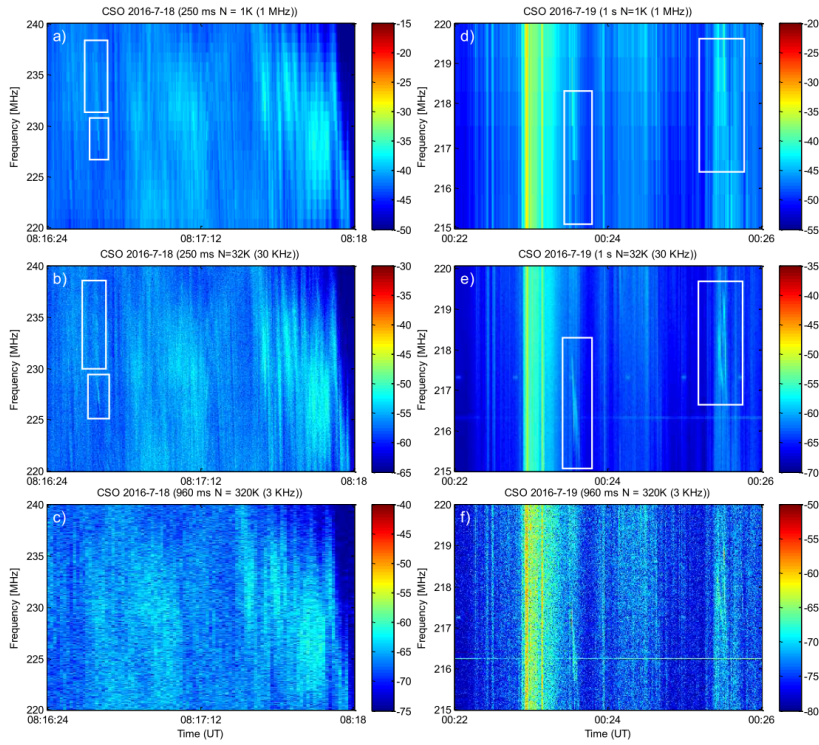

Fig. 6 Two events observed on 2016 July 18 (a–c) and 2016 July 19 (d–f). The contrast levels of the spectra with different N have been adjusted to reveal similar color of the background emission. The FFT word length N is taken to be 1 k, 32 k, and 320 k for the upper, middle and lower panels, respectively, with different temporal resolutions. The time resolutions of the left panels are 250 ms (a, b) and 960 ms (c), and the time resolutions of the right panels are 1 s (d, e) and 960 ms (f). The white rectangles outline areas of interest.

Figure 7 is a comparison of the dynamic spectra with different temporal resolutions ($\Delta t = 1$ s for panel (a) and $\Delta t = 10$ ms for panel (b)), and the same spectral resolution (1 MHz). We see that the mosaic patterns are present in Figure 7(a) with a lower temporal resolution while they disappear in Figure 7(b) with a higher tempo-

ral resolution. In addition, in Figure 7(b) a lot of drifting fine-filamentary spectral structures are present.

In summary, with the above comparisons of dynamic spectra with different spectral and temporal resolutions, we show the potential capability of using different combinations of temporal and spectral resolutions in investi-
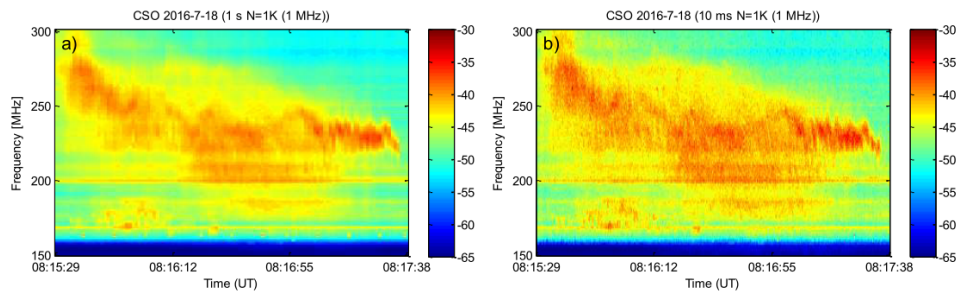
Fig. 7 Dynamics spectra with different temporal resolutions: (a) $\Delta t = 1\,\mathrm{s}$ and (b) $\Delta t = 10\,\mathrm{ms}$, using the same spectral resolution ($\Delta f = 1\,\mathrm{MHz}$).

gating the fine spectral structures of a radio burst. This capability will be especially useful when details of fine spectral structures are under study.

5 CONCLUSIONS

There are dozens of solar radio spectrographs around the world that provide continuous data on dynamic spectra of solar radio bursts. These data contain important information about energetic electrons and relevant processes of solar eruptions, particle acceleration through shocks or magnetic reconnection and electromagnetic radiations. Some spectrographs were built one to two decades ago with electronic and digital technologies that suffer from serious limitations. In addition, most systems provide data at fixed spectral and temporal resolutions. Here we present a novel design for a solar radio spectrograph, characterized by the real-time storage of radio intensity data in the time domain and further off-line analysis of the dynamic spectra with user-defined flexible temporal and spectral resolutions. With off-line analysis, the system can achieve a frequency resolution of 3 kHz, which, to the best of our knowledge, is the highest resolution ever reported. The spectrograph was installed at CSO, which has the advantage of very low radio interference. This allows the system to work properly and record clean details of solar radio bursts at metric wavelength.

The system runs in two modes: normal mode and burst mode, determined automatically with a prescribed threshold of total intensity. The merit of the design is demonstrated with a detailed analysis of two radio burst events recorded by the CSO spectrograph. Calibration methods of the system are also briefly introduced. The design of the spectrograph enables great flexibility in the analysis of solar radio bursts. It is particularly helpful when specific fine spectral structures are of major interest, which can be easily missed from detection if the spectral-temporal resolutions were fixed, as is usually done with other spectrographs.

References

Benz, A. O., Monstein, C., & Meyer, H. 2005, Sol. Phys., 226, 143

Benz, A. O., Monstein, C., Meyer, H., et al. 2009, Earth Moon and Planets, 104, 277

Chen, Y., Du, G., Feng, L., et al. 2014, ApJ, 787, 59

Du, G., Chen, Y., Lv, M., et al. 2014, ApJ, 793, L39

Du, G., Kong, X., Chen, Y., et al. 2015, ApJ, 812, 52

Feng, S. W., Chen, Y., Kong, X. L., et al. 2013, ApJ, 767, 29

Feng, S. W., Chen, Y., Song, H. Q., Wang, B., & Kong, X. L. 2016, ApJ, 827, L9

Feng, S. W., Du, G. H., Chen, Y., et al. 2015, Sol. Phys., 290, 1195

Fu, Q., Ji, H., Qin, Z., et al. 2004, Sol. Phys., 222, 167

Gao, G., Wang, M., Dong, L., Wu, N., & Lin, J. 2014, New Astron., 30, 68

Gao, G., Wang, M., Wu, N., et al. 2016, Sol. Phys., 291, 3369

Kondo, T., Isobe, T., Igi, S., Watari, S.-I., & Tokumaru, M. 1994, Communications Research Laboratory Review, 40, 85

Kong, X. L., Chen, Y., Li, G., et al. 2012, ApJ, 750, 158

Kong, X., Chen, Y., Feng, S., et al. 2016, ApJ, 830, 37

Koval, A., Stanislavsky, A., Chen, Y., et al. 2016, ApJ, 826, 125

McLean, D. J., & Labrum, N. R. 1985, Solar Radiophysics: Studies of Emission from the Sun at Metre Wavelengths (Cambridge: Cambridge Univ. Press)

Melrose, D. B. 1980, Plasma Astrophysics. Nonthermal Processes in Diffuse Magnetized Plasmas - 1: The Emission, Absorption and Transfer of Waves in Plasmas; 2: Astrophysical Applications (New York: Gordon and Breach)

Tan, C., Yan, Y., Tan, B., et al. 2015, ApJ, 808, 61

Vasanth, V., Chen, Y., Feng, S., et al. 2016, ApJ, 830, L2

Wild, J. P., & McCready, L. L. 1950, Australian Journal of Scientific Research A Physical Sciences, 3, 387